

# Electrothermal Simulation of the Production of Alumina by Spark Plasma Sintering

Mustafa Guven GOK 

<sup>1</sup>Gaziantep University, Department of Metallurgical and Materials Engineering, Gaziantep, Turkiye

## Abstract

Although the spark plasma sintering (SPS) method is a very advantageous technique in many aspects, the inability to clearly read the temperature formed on the material during sintering and heterogeneous temperature distributions are the biggest problems of this process. Therefore, it is a common situation that samples taken from different regions of the produced material have different densities and mechanical properties. In this study, the temperature distributions, current density and joule heating effect of the entire setup consisting of the alumina ( $Al_2O_3$ ) sample to be sintered, inconel electrodes, graphite dies, punches and spacers, as well as the critical regions in this setup, are modeled by using finite element software. According to the results, the temperature is maximum at the centre of the  $Al_2O_3$  sample and the temperature gradient along its radius is  $22.4^\circ C$ . The temperature difference between the inner wall of the hole which is opened in the graphite mold to measure the sintering temperature and the centre of the  $Al_2O_3$  sample is around  $40^\circ C$ . In addition, during the SPS process,  $Al_2O_3$  is not heated directly by the joule effect and the temperature gradient in the sample occurs due to mold surface radiation.

**Keywords:** Finite Element Analysis, Spark Plasma Sintering, Alumina, Powder Metallurgy

## I. INTRODUCTION

Although the production of materials from powder by the traditional sintering method (moulding/pressure and sintering processes are done separately) has been known for many years, the most important progress in this regard began with the development of technologies in which molding-pressure and heating processes are performed simultaneously [1]. In the powder metallurgy process, simultaneous application of temperature and pressure offers great advantages for sintering various materials. Spark plasma sintering (SPS) and Hot pressing (HP) are the best examples of processes where temperature and pressure are applied simultaneously [2]. In fact, SPS and HP processes are similar to each other. But the main difference is the mechanisms involved in generating heat and transmitting it to the material to be sintered. An external heating source is used in the HP process. However, in the SPS process, a direct current is provided to pass through the sample to be sintered and/or the conductive (usually graphite) die. This direct current is pulsed and controllable. In this way, the direct current, which has a pulsed character, creates an electric field during the SPS process and the powders are heated up both internally and externally [2–5]. The heat is generated directly in the material to be sintered or in the molds, and in very short periods of time, the temperature of the sample can be equalized to the sintering temperature values. Thanks to this high heating rate, the microstructure of the material (eg grain size) can be easily kept under control [5–10].

A typical SPS machine consists of a DC pulse generator, electrodes, uniaxial press, vacuum chamber, and some measuring components. Thanks to the spark plasma, DC pulse discharge, Joule heating and the diffusion effect of an electric field are created. In addition, simultaneous pressure application creates plastic flow in the material. The sintering temperature is kept under control by adjusting the pulse duration, ramp rate, voltage and pulse current before or during the process. In the first stage of the process, the gases are removed and a vacuum environment is created. Then, pressure and resistance heating are applied respectively and cooling process is carried out in the last step. When a discharge of the spark occurs during the process at the contact point of the particles of the material or in the space between the particles, the temperature in these areas can rise to thousands of degrees celsius momentarily. Thus, melting and evaporation occur on the surface region of the particles and sintering necks are come into existence between the particles. In addition, the concurrent application of current and pressure causes an increase in the rate of heating. This decreases both the sintering temperature and time, allowing consolidation without excessive grain growth. In addition to these advantages, there is no need to use binders in the SPS process and does not require a pre-compression process. The material powder to be sintered is directly filled into a graphite mold and a material with high theoretical density values with superior mechanical properties can be produced [11,12].

However, in addition to all these advantages, heterogeneous temperature distribution in the SPS process is a very common problem. Since the sintering temperature is read from the graphite die surface, it is significant to know how the temperature is distributed throughout the sintered material section.

**Corresponding Author:** MUSTAFA GUVEN GOK, Tel: 0342 360 12 00-dahili-3931, e-mail: mggok@gantep.edu.tr

**Submitted:** 25.11.2023, **Revised:** 09.12.2023, **Accepted:** 07.02.2024

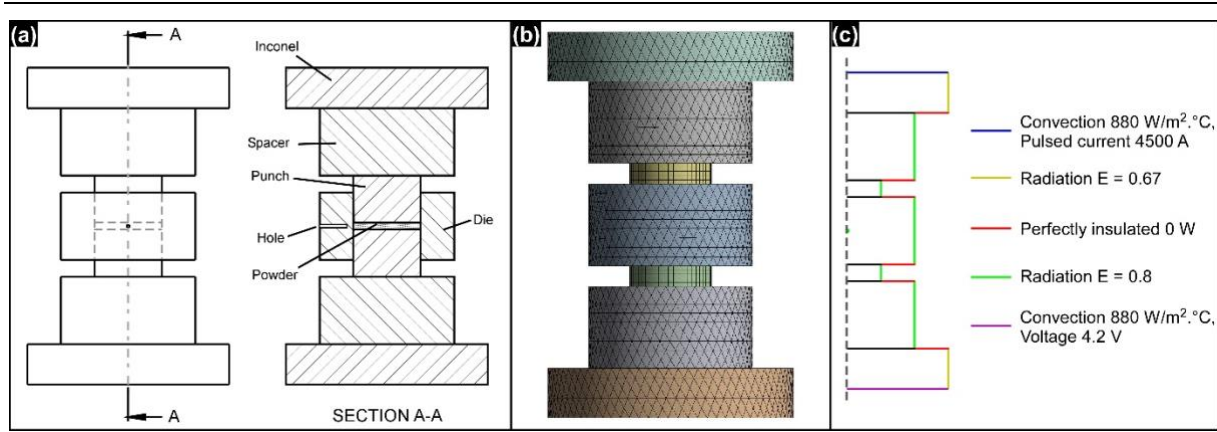


**Figure 1.** (a) assembly of system, (b) meshes and (c) boundary conditions.

Because the temperature distribution during sintering has a significant impact on the mechanical properties, homogeneity and microstructure of the produced material. For example, Sahin et al. [13] produced B<sub>4</sub>C-based ceramic materials with the SPS method and determined that there were density differences between the edges and centers of the samples they produced. One way to predict the temperature distribution across the material cross section during sintering is through finite element analysis (FEA). Therefore, in this study, finite element modeling (FEM) of the SPS technique was made to understand the temperature distributions along the cross section of the mold and sintered material in the production of monolithic alumina by SPS method.

## II. MATERIALS AND METHODS

### 2.1. Definition of geometry

In this study, the simulation of the heating process of an Al<sub>2</sub>O<sub>3</sub> sample during the SPS process was performed using Thermal-Electric module of the ANSYS® software. The technical drawing of the assembly consisting of graphite dies, punches, spacers, electrodes and the material to be sintered is given in Figure 1 (a). Dimensional values of these parts were given in Table 1. As can be understood from the system, Al<sub>2</sub>O<sub>3</sub> powder is placed in the mold cavity of the graphite mold.

**Table 1.** Dimensions of the SPS system.

Part	Dimensions (mm)	
	Diameter	Height
Specimen	50	5
Punch	50	35
Die	100	50
Spacer	100	50
Inconel	150	30

There were two graphite punches above and below the Al<sub>2</sub>O<sub>3</sub> powder. At both ends of the system were Inconel (a kind of nickel-chromium alloy) electrodes in contact with a liquid at constant temperature. Graphite spacers were placed between the electrodes and the punches. In addition, a hole having a diameter of 2 mm and a depth of 20 mm was drilled in the

middle of the graphite mold so that the temperature could be read during sintering.

### 2.2. Mesh and Boundary conditions

In this study, the simulation of SPS process of the Al<sub>2</sub>O<sub>3</sub> sample was performed using Thermal-Electric module of the ANSYS® software. The assembly created after the solid modeling drawings was transferred to Ansys Workbench finite element analysis (FEA) software. Different mesh sizes and shapes were tried to achieve mesh independence and accordingly 3D tetrahedral (in inconel, graphite molds and spacers) and hexahedral (in punch and sample) were used. The total mesh nodes and elements numbers were 186172 and 116720, respectively. After the meshing process, the finite element model of the system is given in Figure 1 (b). It was assumed that radiative heat transfer occurred between the atmosphere of the SPS chamber and the surfaces.

On the other hand, convective heat transfer on the vertical walls was ignored. Additionally, the contact resistance between the interfaces of the constituents was neglected. The applied boundary conditions are schematically summed up in Figure 1 (c).

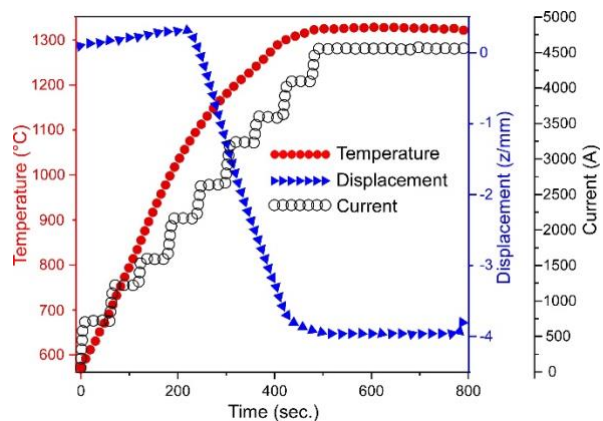


**Figure 2.** Graphs of experimental results showing the measured temperature, displacement, and applied electric current during the SPS process of Al<sub>2</sub>O<sub>3</sub>.

To calculate the temperature distribution during the process of SPS, 4500A pulsed electrical current

**Table 2.** Temperature dependent material properties (T=Kelvin).

Material	Inconel [14,15]	Graphite [15–17]	Al <sub>2</sub> O <sub>3</sub> [14,15]
Thermal conductivity (W/m·K)	$10.03 + 0.0157 \times T$	$82.85 - 0.06 \times T + 2.58 \times 10^{-5} \times T^2$	$39500 \times T^{-1.26}$
Electric resistivity ( $\Omega \cdot m$ )	$9.82 \times 10^{-7} + 1.6 \times 10^{-7} \times T$	$2.14 \times 10^{-5} - 1.34 \times 10^{-8} \times T + 4.42 \times 10^{-12} \times T^2$	$8.7 \times 10^9 \times T^{-4.82}$
Density (kg/m <sup>3</sup> )	8430	$1904 - 0.01414 \times T$	3899

directly applied to the system. Because in the experimental study using a 20000A capacity SPS device (SPS Syntex Inc., 7.40 MK-VII), approximately 4500A electric current was applied to reach the sintering temperature of Al<sub>2</sub>O<sub>3</sub> (see Figure 2). The sintering temperature (approximately 1300°C) was the temperature at which shrinkage was completed.

### 2.3. Material Properties

Thermoelectric analyzes are directly related to electrical and thermal properties. The change in the properties of the material in this case is a function of temperature. Therefore, the formulas regarding the physical properties of the materials in the assembly are presented in Table 2. In addition, all graphite elements in this study were assumed to be isotropic, that is, all physical properties were the same in all directions.

## III. RESULTS AND DISCUSSION

### 3.1. Temperature distribution analyses

Figure 3 shows the temperature contours for the system consisting of inconel electrodes, graphite dies, and Al<sub>2</sub>O<sub>3</sub> sample during the spark plasma sintering process.

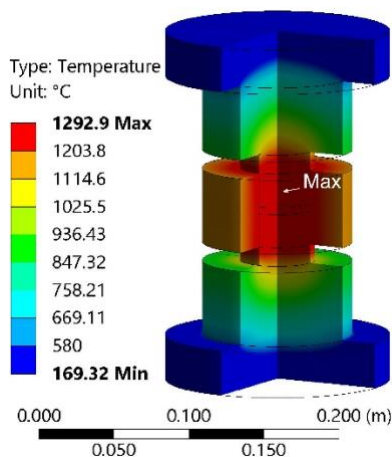


**Figure 3.** Temperature distribution inside the all components of system.

This figure is given as a partial cross-sectional view in order to determine the temperature distributions inside the all components of the system. As can be understood, under the defined boundary conditions, the maximum temperature of the system was 1292.9 °C. This maximum temperature point was at the centre of the upper graphite punch. Under the next heading,

by explaining the joule heating and current density phenomena, it will be understood why the maximum temperature is in the graphite punch. as a matter of fact, when the counter is examined in detail, it can be understood that the centre of the sintered Al<sub>2</sub>O<sub>3</sub> sample is almost at the maximum temperature value. It is also seen that the temperature distribution is highest in the central regions of all system parts.

The distribution of temperature along the diameter of the alumina sample is seen in the Figure 4 (a) and (b). The maximum temperature on the sample was about 1288.6 °C. Additionally, the center of the sample was at the maximum temperature value. As seen in the Figure 4 (b), the minimum temperature was 1260.2 °C and it was at the edges of the Al<sub>2</sub>O<sub>3</sub> sample close to the graphite die. Temperature gradient ( $\Delta T$ ) on the specimen was 22.4 °C. Also, there was no important temperature difference across the sample height.

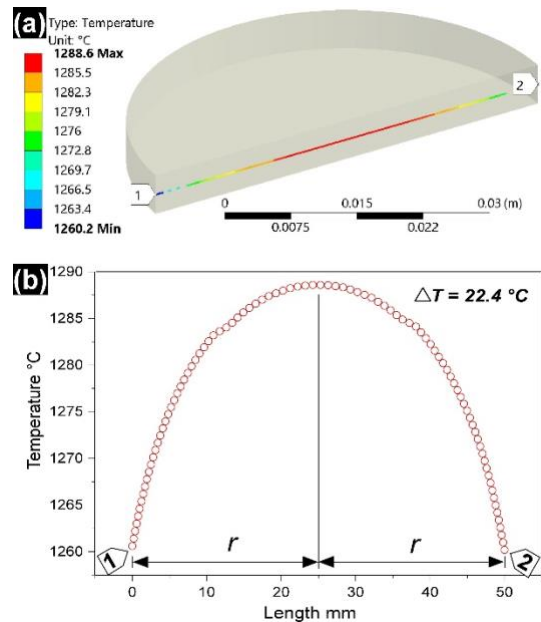


**Figure 4.** Temperature distribution along the diameter of the Al<sub>2</sub>O<sub>3</sub> sample as (a) contours and (b) graph.

When the temperature gradient between the inner wall of mold hole and the centre of sample is examined, it can be figured out that the temperature on the inner wall of mold hole which is opened to measure the sintering temperature is 1250.3 °C (see Figure 5 (a) and (b)). The mentioned temperature gradient is more clearly understood in the graph given in Figure 5 (b). The temperature gradient from the inner wall of the

mold hole to the center of the sample is 38.3 °C. This means that there is a difference of about 40 °C in

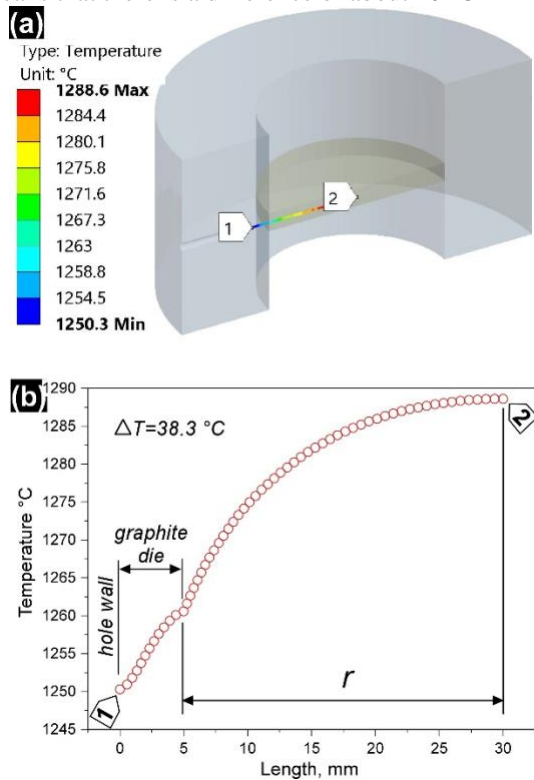


**Figure 5.** Temperature distribution from the inner wall of the die hole to the center of the Al<sub>2</sub>O<sub>3</sub> as (a) contours and (b) graph.

between the actual temperature at the center of the sample and the sintering temperature read from the SPS device. This difference has great importance. Because during spark plasma sintering, the temperature measured from this inner wall of the hole is considered as the sintering temperature.

During experimental procedures, an optical pyrometer is usually placed outside the SPS chamber, and thanks to this pyrometer, the sintering temperature data on the wall surface of the hole opened in the graphite mold is read through a window on the chamber wall. Therefore, it is important to know that temperature

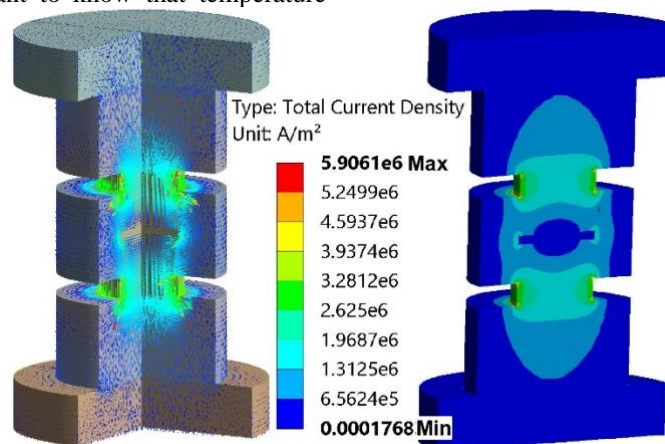


**Figure 7.** Total current density in the all components of system.

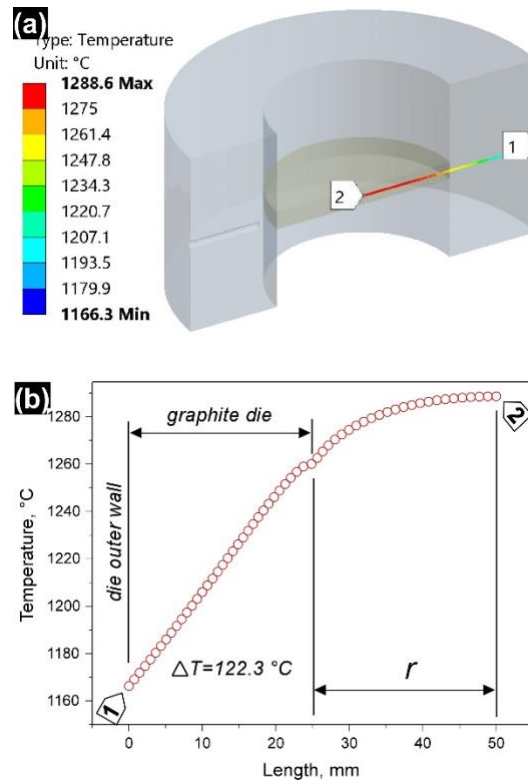


**Figure 6.** Temperature distribution from the outermost wall of the die to the center of Al<sub>2</sub>O<sub>3</sub> as (a) contours and (b) graph.

difference between the observed sintering temperature and the actual temperature during the sintering of Al<sub>2</sub>O<sub>3</sub> using the SPS method is about 40°C. The temperature difference from the outer wall of the mold to the center of the sample during SPS process of Al<sub>2</sub>O<sub>3</sub> is given in Figure 6 (a) and (b). Clearly, in this case the temperature difference ( $\Delta T$ ) is approximately 122.3 °C. Moreover, there is a temperature difference of around 94 °C in between the outer (on the sintered sample side) and inner wall of the graphite die. These significant temperature differences are caused by heat flow from the outermost wall of the graphite die to the spark plasma chamber or carbon belt.

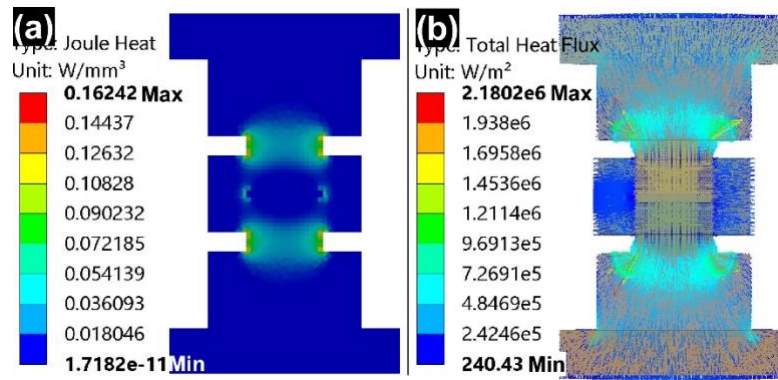


**Figure 8.** (a) Joule heating and (b) total heat flux distributions in the all components of system.

### 3.2. Current density, joule heating and total heat flux analyses

Figure 7 shows the total current density ( $A/m^2$ ) on the Inconel electrodes, graphite die, spacer, punches, and  $Al_2O_3$  sample. It is immediately obvious that the electric current does not exhibit a uniform distribution. Since alumina is an electrically non-conductive material, no electric current flows through the  $Al_2O_3$  sample. An almost identical situation was shown in the study by Sakkaki et al [15]. The electric current density was maximum ( $5.96 \times 10^6 A/m^2$ ) in the graphite punch. Therefore, this explains why the maximum temperature ( $1292.9^\circ C$ ) occurs in the graphite punch.

On the other hand, as seen in Figure 8 (a), joule heating was at the maximum level ( $0.1624 W/mm^3$ ) in the graphite punch. This situation, together with those mentioned above, explains why graphite punch failure often occurs during SPS process of non-conductive ceramic material. If an electrically conductive material were produced with the SPS process, the maximum joule heat and maximum current density would most likely occur in the sample. Additionally, another high joule heat region is formed in the graphite die-edge region of  $Al_2O_3$  sample. In this case, as expected, there was no direct joule heating during SPS process of the alumina sample. Instead, the heat generated in the punches and graphite die was quickly and efficiently transferred to the alumina sample by conduction. In fact, it is reported that this phenomenon creates less thermal gradient in the material during the SPS process of non-conductive materials compared to conductive ones [15,18]. In addition, it can be easily understood from Figure 8 (b) that there is an intense heat flux from the graphite die surface to the chamber due to radiation. Therefore, heat loss occurred due to surface radiation of the graphite die. This phenomenon cooled the edge region of the  $Al_2O_3$  sample and a temperature gradient was formed.

### IV. CONCLUSIONS

In this study, FEM study was performed to better understand the temperature distributions during the production of  $Al_2O_3$  with the SPS technique. As a result, when the defined boundary conditions and

4500A electric current were applied to the system, the following important results were obtained.

- The maximum temperature occurring in the  $Al_2O_3$  sample is at the center of the sample and is  $1288.6^\circ C$ .
- The temperature gradient across the  $Al_2O_3$  sample is  $22.4^\circ C$ .
- There is a difference of around  $40^\circ C$  between the center  $Al_2O_3$  sample and inner wall of the die hole.
- The temperature difference from the outermost surface of the graphite die to the center of the  $Al_2O_3$  sample is approximately  $122^\circ C$ .
- Total current density and joule heating effect are maximum in graphite punches.
- During spark plasma sintering,  $Al_2O_3$  is heated not directly by the Joule effect but by thermal conduction. The temperature in the  $Al_2O_3$  sample increases due to heat conduction from the graphite die and punches.
- Heat loss occurs at the edges of the sample due to mold surface radiation, resulting in a temperature gradient in the  $Al_2O_3$  sample.

### REFERENCES

- [1] Laszkiewicz-Łukasik, J., Putyra, P., Klimczyk, P., Podsiadło, M., Bednarczyk, K., (2021). Spark Plasma Sintering/Field Assisted Sintering Technique as a Universal Method for the Synthesis, Densification and Bonding Processes for Metal, Ceramic and Composite Materials. *Journal of Applied Materials Engineering*. 60(2): 53–69.
- [2] Cavaliere, P., Sadeghi, B., Shabani, A., (2019). Spark Plasma Sintering: Process Fundamentals. Spark Plasma Sintering of Materials, *Cham: Springer International Publishing* p. 3–20.
- [3] Anselmi-Tamburini, U., (2021). Spark Plasma Sintering. Encyclopedia of Materials: Technical Ceramics and Glasses, *Elsevier* p. 294–310.
- [4] Bubesh Kumar, D., Selva babu, B., Aravind Jerrin, K.M., Joseph, N., Jiss, A., (2020). Review of Spark Plasma Sintering Process. *IOP*

- Conference Series: Materials Science and Engineering*. 993(1): 012004.
- [5] Gok, M.G., (2021). Spark Plasma Sintering of Nano Silicon Carbide Reinforced Alumina Ceramic Composites. *European Mechanical Science*. 5(2): 64–70.
- [6] Razavi, M., Farajipour, A.R., Zakeri, M., Rahimpour, M.R., Firouzbakht, A.R., (2017). Production of Al<sub>2</sub>O<sub>3</sub>–SiC nano-composites by spark plasma sintering. *Boletín de La Sociedad Española de Cerámica y Vidrio*. 56(4): 186–94.
- [7] Álvarez, I., Torrecillas, R., Solis, W., Peretyagin, P., Fernández, A., (2016). Microstructural design of Al<sub>2</sub>O<sub>3</sub>–SiC nanocomposites by Spark Plasma Sintering. *Ceramics International*. 42(15): 17248–53.
- [8] Cetinbag, A., Ormanci, O., Goller, G., (2022). Production of B<sub>4</sub>C reinforced TZM alloy and boriding its surface in one step by spark plasma sintering (SPS). *International Journal of Refractory Metals and Hard Materials*. 106: 105860.
- [9] Danisman, C.B., Goller, G., (2023). Spark plasma sintered mn-al (magnets) production and characterization with experimental design. *Archives of Metallurgy and Materials*. 68(4): 13571367.
- [10] Kaplan Akarsu, M., Akin, I., Sahin, F., Goller, G., (2022). Comparative study of reactive and nonreactive spark plasma sintering routes for the production of TaB<sub>2</sub>-TaC composites. *International Journal of Applied Ceramic Technology*. 19(1): 332–43.
- [11] Saheb, N., Iqbal, Z., Khalil, A., Hakeem, A.S., Al Aqeeli, N., Laoui, T., et al., (2012). Spark Plasma Sintering of Metals and Metal Matrix Nanocomposites: A Review. *Journal of Nanomaterials*. 2012: 1–13.
- [12] Akin, I., (2010). ZrB<sub>2</sub> esaslı kompozitlerin spark plazma sinterleme (SPS) yöntemi ile üretimi ve karakterizasyonu / Production and characterization of ZrB<sub>2</sub> based composites prepared by spark plasma sintering. Istanbul Technical University, (2010).
- [13] Çınar Şahin, F., Mansoor, M., Cengiz, M., Apak, B., Yanmaz, L., Balazsi, K., et al., (2022). B<sub>4</sub>C Composites with a TiB<sub>2</sub>-C Core–Shell Microstructure Produced by Self-Propagating High-Temperature Synthesis-Assisted Spark Plasma Sintering. *The Journal of Physical Chemistry C*. 126(47): 20114–26.
- [14] Pavia, A., Durand, L., Ajustron, F., Bley, V., Chevallier, G., Peigney, A., et al., (2013). Electro-thermal measurements and finite element method simulations of a spark plasma sintering device. *Journal of Materials Processing Technology*. 213(8): 1327–36.
- [15] Sakkaki, M., Sadegh Moghanlou, F., Vajdi, M., Shahedi Asl, M., Mohammadi, M., Shokouhimehr, M., (2020). Numerical simulation of heat transfer during spark plasma sintering of zirconium diboride. *Ceramics International*. 46(4): 4998–5007.
- [16] Manière, C., Pavia, A., Durand, L., Chevallier, G., Afanga, K., Estournès, C., (2016). Finite-element modeling of the electro-thermal contacts in the spark plasma sintering process. *Journal of the European Ceramic Society*. 36(3): 741–8.
- [17] Molénat, G., Durand, L., Galy, J., Couret, A., (2010). Temperature Control in Spark Plasma Sintering: An FEM Approach. *Journal of Metallurgy*. 2010: 1–9.
- [18] Vanmeensel, K., Laptev, A., Hennicke, J., Vleugels, J., Vanderbiest, O., (2005). Modelling of the temperature distribution during field assisted sintering. *Acta Materialia*. 53(16): 4379–88.